

AperTO - Archivio Istituzionale Open Access dell'Università di Torino

## Structural characterization of 8 MeV 11B implanted diamond

### This is the author's manuscript

*Original Citation:*

*Availability:*

This version is available <http://hdl.handle.net/2318/1732691> since 2020-03-04T09:21:54Z

*Published version:*

DOI:10.1016/j.diamond.2020.107770

*Terms of use:*

Open Access

Anyone can freely access the full text of works made available as "Open Access". Works made available under a Creative Commons license can be used according to the terms and conditions of said license. Use of all other works requires consent of the right holder (author or publisher) if not exempted from copyright protection by the applicable law.

(Article begins on next page)

# Structural characterization of 8 MeV $^{11}\text{B}$ implanted diamond

P. Aprà<sup>1,2</sup>, J. Ripoll-Sau<sup>3</sup>, J. Manzano-Santamaría<sup>4</sup>, C. Munuera<sup>5</sup>, J. Forneris<sup>1,2</sup>, S. Ditalia Tchernij<sup>1,2</sup>,  
P. Olivero<sup>1,2</sup>, F. Picollo<sup>1,2,\*</sup>, E. Vittone<sup>1,2</sup>, M. D. Ynsa<sup>3,6</sup>

<sup>1</sup> Physics Department and “NIS” inter-department centre, University of Torino, Torino, Italy

<sup>2</sup> Italian Institute of Nuclear Physics, section of Torino, Torino, Italy

<sup>3</sup> Departamento de Física Aplicada and Centro de Microanálisis de Materiales (CMAM),  
Universidad Autónoma de Madrid, Madrid, Spain

<sup>4</sup> Dept. de Matemática Aplicada, Ciencia e Ingeniería de Materiales y Tecnología Electrónica,  
ESCET, Universidad Rey Juan Carlos., C/ Tulipán s/n, Móstoles 28933, Madrid, Spain

<sup>5</sup> Instituto de Ciencia de Materiales de Madrid (ICMM), Consejo Superior de Investigaciones  
Científicas (CSIC), Madrid, Spain

<sup>6</sup> Instituto de Ciencia de Materiales Nicolás Cabrera, Universidad Autónoma de Madrid, Madrid,  
Spain

\*Corresponding author. Email: federico.picollo@unito.it

## Abstract

Boron is the most effective dopant element in diamond and the capability to introduce high densities of boron makes ion implantation a potential key technology to verify superconductivity in diamond. However, its optimization involves many experimental parameters (i.e. ion energy, fluence, current, annealing times and temperature) and the effectiveness of B implantation to induce superconductivity in diamond is still to be demonstrated. So far, a limited number of works in the range of high (i.e. >5 MeV) B ion energies have been carried, despite the promising perspective offered by deep implantation to fabricate sub-superficial superconductive structures in diamond. To this scope, in the present work, we report on the study of the structural effects of high-energy boron ion irradiation on diamond. Monocrystalline diamond sample was irradiated with an 8 MeV  $^{11}\text{B}$  microbeam across multiple square areas, characterized by a different combination of fluences and ion currents. After the implantation, the sample was characterized by Raman spectroscopy and Atomic Force Microscopy to assess its structural modifications and the related surface swelling. Significant variations related to the irradiation condition have been determined.

## 1. Introduction

Diamond doping at very high concentrations represents a challenging process, in particular because of the high diffusion, but it opens to technologically appealing applications such as the fabrication of semiconducting and superconducting devices in an extreme material operating at high temperatures. In particular, Moussa and Cohen [1] theoretically predicted that heavily boron doped diamond without electronically compensating defects (i.e. boron concentrations of 20% - 30%) should display a superconducting behavior with a critical temperature above 80 K, but up to now optimal crystal synthesis conditions were not achieved yet. Alternative strategies are under study for the incorporation of substitutional boron atoms at very high concentrations within the diamond lattice, thus overcoming the limits of chemical vapor deposition growth. MeV ion beam implantation has proven to represent a promising route, allowing the creation of semiconducting

sub-superficial highly-B-doped layers [2–4]. The observation of the superconducting charge transport mechanisms in strongly-B-doped diamond via ion implantation requires specific strategies to minimize collateral structural damage effects which are critically detrimental. These collateral effects occur in correspondence of the depth at which the ions are implanted at the highest concentration, i.e. the end-of-range damage peak. In the specific case of B doping in diamond, these collateral defects dramatically affect the electrical conduction properties of the material, thus limiting the predicted increase of the superconducting transition temperature, since vacancies or interstitial boron atoms act as compensating defects [4,5].

Moreover, the progressive defect accumulation in diamond promotes a phase transition of the damaged area to graphite after high temperature annealing when a critical vacancy density (usually referred as graphitization threshold, generally ranging within  $2\text{--}6 \times 10^{22}$  vacancies  $\text{cm}^{-3}$  [6–9]) is reached. On the other hand, regions implanted below this critical value restore to a large extent the pristine diamond structure since a large fraction of the Frenkel pair defects recombine upon thermal treatment [10]. In this context, if suitably assessed, MeV ion irradiation would offer appealing perspectives with respect to the more readily available and widely employed ion irradiation processing carried in the keV energy range [2,11,12]. Firstly, the possibility of creating deep sub-superficial structures offered by the use of high-energy ions would allow a higher degree of integration in the engineering of embedded superconductive structures in a 3D geometry, with potential impact in specific applications such as for example the design of SQUID (superconducting quantum interference devices) devices integrated with MEMS (microelectromechanical systems) structures [13]. Secondly, the formation of high-density doped layers at micrometer depths below the surface could in principle benefit from the strong internal pressures exerted by the surrounding diamond lattice that would pose a constraint to the formation of defect clusters, which are in turn detrimental to superconductive charge transfer. Such an hypothesis is based on the commonly observed evidence of a substantial increase in the above-mentioned graphitization threshold value at increasing depths within the bulk crystal [6–9], and its implications go beyond the issue of superconductivity engineering in diamond via B implantation, since they invest also the complex issue of the management of damage accumulation in diamond irradiation and concurrent annealing [14–16]. In this framework, the assessment of the structural defects introduced into the crystal upon high-energy B irradiation becomes of crucial importance and Raman spectroscopy can provide a significant insight in this respect [17–21].

In the present work, we report on systematic Atomic Force Microscopy (AFM) and Raman spectroscopy characterization of 8 MeV boron implanted diamond with different combination of fluences and ion currents, both before and after high-temperature annealing. In the former set of measurements, the mechanical distortion of the diamond structure occurring at the sample surface was investigated with a specific focus on edge effects, while in the latter one the structural modifications of the damaged crystal were correlated with different irradiation conditions. This study allowed the investigation of a range of implantation parameters both before and after high temperature annealing that so far had not been explored in literature: more specifically, a high ion energy was selected, since it would allow the creation of deeper (i.e.  $>4\text{ }\mu\text{m}$ ) sub-superficial highly-B-doped regions, with promising perspectives in the fabrication of integrated superconducting devices.

## 2. Materials and methods

The sample employed in this study is a high-purity (“optical grade”) monocrystalline diamond, produced with Chemical Vapour Deposition by ElementSix™. The crystal has a (100) crystallographic orientation, is  $3 \times 3 \times 0.4\text{ mm}^3$  in size and it is classified as type IIa, being

characterized by concentrations of single substitutional nitrogen and boron smaller than 10 ppm and 5 ppb, respectively.

The sample was implanted, following a previously adopted protocol [22], using the microbeam line of the “Center for Micro Analysis of Materials” (CMAM) at the Autonomous University of Madrid, by using a focused 8 MeV  $^{11}\text{B}$  ion beam with a spot size of  $5 \times 5 \mu\text{m}^2$ . 12 different square-shaped areas of  $\sim 100 \times 100 \mu\text{m}^2$  size were irradiated at different combinations of fluences and ion currents. More precisely, 9 areas (labeled as A-I, see Table 1) were implanted at fixed ion current of 500 pA (corresponding to an estimated fluence rate of  $12.5 \times 10^{15} \text{ cm}^{-2} \text{ s}^{-1}$ ) and fluences ranging from  $1 \times 10^{15} \text{ cm}^{-2}$  to  $4.4 \times 10^{16} \text{ cm}^{-2}$ , while other 3 areas (labeled as J-L, see Table 1) were implanted at fixed fluence of  $1 \times 10^{16} \text{ cm}^{-2}$  and ion currents of 50 pA, 100 pA and 500 pA (fluence rate of  $1.25 \times 10^{15} \text{ cm}^{-2} \text{ s}^{-1}$ ,  $2.5 \times 10^{15} \text{ cm}^{-2} \text{ s}^{-1}$  and  $12.5 \times 10^{15} \text{ cm}^{-2} \text{ s}^{-1}$ , respectively). The irradiation was carried out at room temperature with an angle of incidence of  $0^\circ$ , although a slight misalignment during the set-up assembling could have occurred. The scan was performed on a pixel-by-pixel basis with a spiral pattern by moving the beam position to the next pixel once the designated fluence was achieved.

Region label	Current (pA)	Ion fluence ( $10^{16} \text{ cm}^{-2}$ )	Estimated graphitic layer thickness ( $\mu\text{m}$ )
A	500	0.5	-
B		0.23	-
C		0.1	-
D		4.4	$0.309 \pm 0.019$
E		3.3	$0.46 \pm 0.03$
F		2.1	$0.55 \pm 0.05$
G		0.7	$0.102 \pm 0.018$
H		0.9	$0.142 \pm 0.016$
I		1.2	$0.187 \pm 0.016$
J	50	1	$0.157 \pm 0.014$
K	100	1	$0.157 \pm 0.014$
L	500	1	$0.157 \pm 0.014$

*Table 1: Summary of the irradiated areas and their corresponding fluence, ion current values and the estimated graphitic layer thickness.*

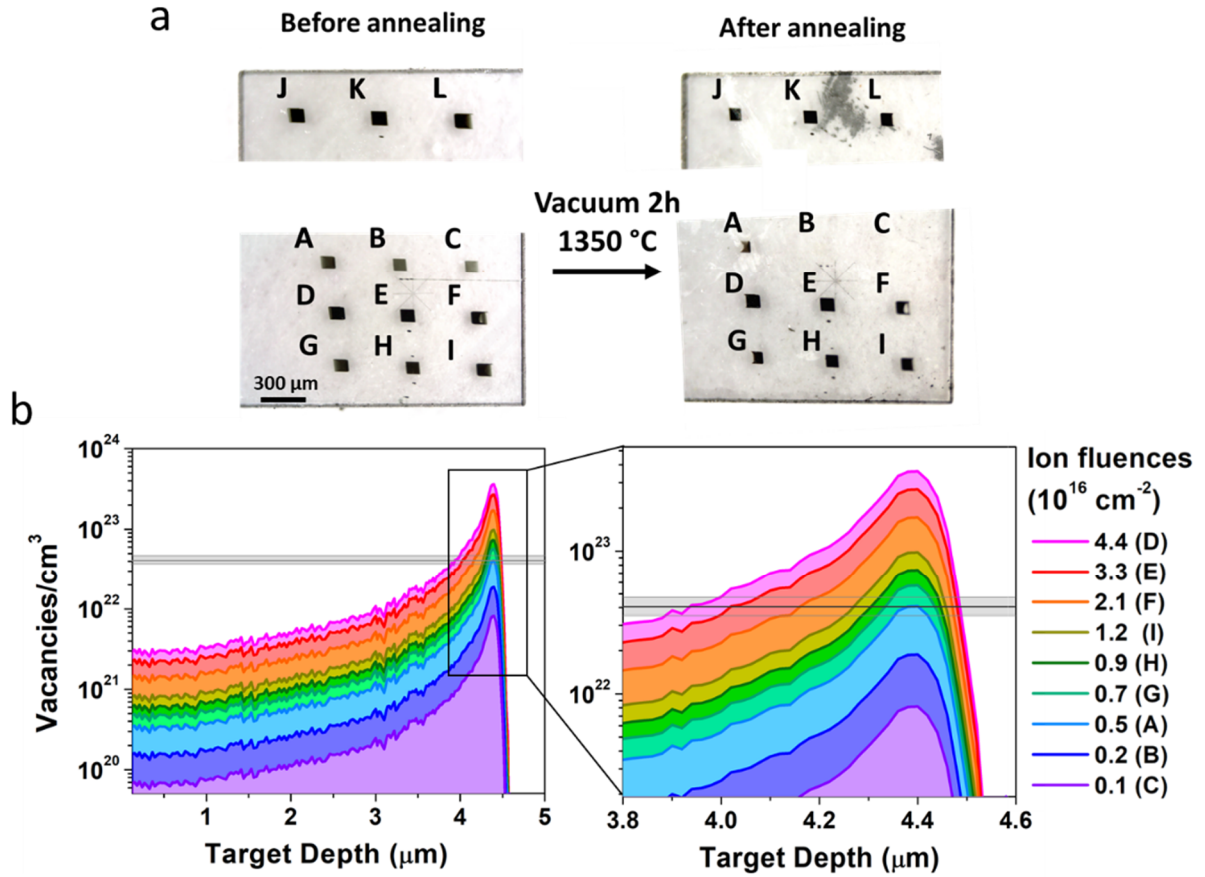


Figure 1 (a) Optical transmission micrographs of the sample before and after the annealing process; the areas are labeled accordingly to what reported in Table 1. (b) Depth profiles of the SRIM-simulated vacancy density, for each employed fluence; the inset reports the zoomed depth region near to the end of range of the ions; in the inset, the horizontal band represents the estimated graphitization threshold (comprised between  $3.7 \times 10^{22}$  vacancies  $\text{cm}^{-3}$  and  $4.5 \times 10^{22}$  vacancies  $\text{cm}^{-3}$ ).

Figure 1a shows optical transmission micrographs of the irradiated areas within the diamond sample, both before and after the thermal annealing. In both micrographs the areas are labeled accordingly to what reported in Table 1.

After ion irradiation, the sample was annealed in high vacuum ( $3 \times 10^{-7}$  mbar pressure) at 1350 °C for 2 hours.

Subsequently, an oxygen plasma cleaning was performed for 15 minutes, to remove the graphitic layers formed at the sample surface during the high temperature annealing. As reported in Figure 1a, all implanted areas are fully converted to graphite upon thermal annealing, with the exception of areas B and C, which were irradiated at the lowest fluences, and thus were re-converted to diamond.

A Monte-Carlo simulation of the ion-induced damage was performed with the 2008 version of the SRIM software [23]. The simulation was run in the “Detailed calculation with full damage cascades” mode by setting a 50 eV displacement energy [24]. The range of 8 MeV  $^{11}\text{B}$  ions is  $\sim 4.4 \mu\text{m}$ , with a maximum value of the linear vacancy density of  $\sim 800$  vacancies  $\mu\text{m}^{-1}$  ion $^{-1}$  in

proximity of the Bragg peak. In Figure 1b we report, for each fluence, the volume density of induced vacancies in function of the depth within the sample, obtained by multiplying the above-mentioned linear density of vacancies with the fluence. This estimation is based on a rough linear approximation that does not consider concurrent complex processes such as self-annealing, ballistic annealing and defect-defect interaction. Despite this rough approximation, the estimated damage density can be still regarded as a useful first-order parameter to assess the thickness of the graphitized layer in samples implanted with different ion species, energies and/or fluences, as reported in previous works [25,26] and confirmed in the present study.

In previous studies, the graphitization threshold related to ion-induced damage was estimated in the  $2\text{--}6 \times 10^{22}$  vacancies  $\text{cm}^{-3}$  range [6–9]. The average value of  $4 \times 10^{22}$   $\text{cm}^{-3}$  roughly corresponds to the maximum vacancy density obtained in the implantation of square A, i.e.  $\sim 4.4 \times 10^{22}$  vacancies  $\text{cm}^{-3}$  (see the light-blue plot in Figure 1b). This is confirmed by the observation that, as shown in Figure 1a, this area is only partially graphitized upon high-temperature annealing, while the regions which are damaged below this threshold re-convert to a diamond phase. As highlighted in the gray horizontal bar reported in the inset of Figure 1b, a 10% uncertainty was associated to the above-mentioned average value of the graphitization threshold, in consideration of both the range of different values reported in literature [6–9] and of the experimental uncertainty associated with the reported fluence values. On this basis, for each area that was irradiated beyond the graphitization threshold, the thickness of the graphitic layer formed upon thermal annealing was estimated by identifying the intersections of the applied graphitization threshold value and the vacancy density plots, while suitably propagating the above-mentioned 10% uncertainty. The resulting thickness estimations are reported in Table 1.

AFM measurements were conducted at the Instituto de Ciencia de Materiales de Madrid (ICMM-CSIC) using a commercial apparatus and software from Nanotec [27] operated at room temperature. The maximum scan area was 80  $\mu\text{m}$ .

Raman spectra were collected with a Horiba Jobin Yvon HR800 Raman micro-spectrometer equipped with a 600 lines  $\text{mm}^{-1}$  diffraction grating, a continuous 532 nm laser excitation beam focused with a 20 $\times$  air objective and a CCD detection system. This setup guarantees the collection of spectra with a spatial resolution of  $\sim 2$   $\mu\text{m}$  in diameter and  $\sim 3$   $\mu\text{m}$  in confocal depth. The spectral resolution is  $\sim 3$   $\text{cm}^{-1}$ . In all measurements the acquisition time for single spot spectra was set to 2 seconds, averaging 3 repeated acquisitions. Single spot Raman spectra were acquired from the center of the implanted areas with the purpose of minimizing effects due to spatial inhomogeneities in the delivered fluence at the edges of the irradiated areas.

### 3 Results

#### 3.1 AFM characterization

The surface topography of as-irradiated areas was characterized by atomic force microscopy (AFM) to assess the swelling effect produced by the constrained expansion of the ion-damage-induced sub-superficial amorphized layer, which is characterized by a lower atomic density with respect to the surrounding diamond matrix [28,29].

Because of the increasing thickness of the amorphized layer, the implanted regions showed an increasing swelling with respect to the fluence. This dependence is more pronounced for the increased swelling occurring at the edges of the implanted areas. Figure 2 shows the topography map (Figure 2a) and the corresponding cross-sectional profile (Figure 2b) of the edge of the area that was implanted at 500 pA current and  $4.4 \times 10^{16} \text{ cm}^{-2}$  fluence (region D). Although the whole implanted region could not be scanned, the AFM results clearly show higher swelling in correspondence of the edges rather than in the central part of the implanted squares. It is worth remarking that it was theoretically predicted in previous works based on both finite element methods [30], (to a larger extent) on analytical models [31], and more recently measured from regions irradiated with swift heavy ions [32] with a better spatial resolution with respect to previous works, in which the edge effect was negligible [29]. The fact that in the present work the effect is particularly evident appears as indicative of the high spatial resolution in the definition of the lip edges of the implanted regions. It is worth observing that in the above-mentioned work [32], the ion irradiation was carried out by using a collimated beam in which a mask defined the shape of the implanted regions. In our work, a spiral scan was adopted, obtaining (at least from a qualitative point of view) a similar swelling lip. This remark is in our view providing a reasonably robust evidence that the presence of the lip is not due to differences in the dwell time at the borders of the scan with respect to the center of the implanted regions.

In order to relate our result with theoretical predictions, we compared the observed lip with the analytical model reported in [31], where the swelling profile is given by:

$$v(x) = v_0 + e^{\beta x}(c_1 \cos(\beta x) + c_2 \sin(\beta x)) + e^{-\beta x}(c_3 \cos(\beta x) + c_4 \sin(\beta x)) \quad (1)$$

where

$$\beta = \sqrt[4]{\frac{3E_{ac}}{E_d(h+v_0)t^3}} \quad (2)$$

$$v_0 = h \frac{(\rho_d - \rho_{ac})}{\rho_d} \quad (3)$$

Differently from what was reported in [31] (in which the constrained expansion of a sharply defined graphitic region was modelled by considering samples after thermal annealing), in Eqs. 2 and 3  $\beta$  and  $v_0$  were quantified by adopting the Young modulus ( $E_{ac} = 21.38 \text{ GPa}$  and density ( $\rho_{ac} = 2.14 \text{ g cm}^{-3}$ ) of amorphous carbon, since our sample was investigated before thermal annealing. Consistently with what was reported in [31], in Eqs. 2 and 3  $E_d = 1144 \text{ GPa}$  and  $\rho_d = 3.52 \text{ g cm}^{-3}$  are the Young modulus and density of diamond, respectively. In a first approximation, we can consider  $h$  as the thickness of the amorphous carbon layer, estimated as the thickness at which the graphitization threshold is exceeded (see table 1), and  $t$  as the diamond cap-layer thickness, evaluated as the region from the surface where the threshold is not reached. The coefficients  $c_1, c_2, c_3, c_4$  are obtained by applying the boundary conditions  $v(0) = 0$ ,  $v'(0) = 0$ ,  $v(l) = 0$ ,  $v'(l) = 0$  and  $l$  is the irradiated region dimension ( $\sim 100 \text{ }\mu\text{m}$ ). The simulated

swelling function is reported together with the observed AFM profile in Figure 2b. The extension of the “lip” on both Z and X axes is satisfactorily comparable with the expectations, although the overall AFM profile is not fully in line with the theoretical prediction. This can be suitably explained by the fact that the analytical model assumes an elastic foundation characterized by well-defined edges and a uniform spring constant embedded in a pristine diamond matrix. In our case, the AFM analysis was conducted on an unannealed sample and therefore the elastic foundation is characterized by smoother edges with respect to the surrounding partially damaged crystal and mechanical properties varying along with the depth.

The dependence of the “plateau” value of the swelling height from damage density has been extensively investigated in previous works [28,29,32,33]. In order to verify the consistency of our data with previous results obtained for other ion species and energies, we considered the swelling height in function of the “damage integral”, which is defined in [32] as:

$$D_{\text{int}} = \int_0^{Z_{\text{max}}} (1 - e^{-\frac{\Phi \cdot S_n(z)}{a}}) \quad (4)$$

where  $\Phi$  is the fluence,  $S_n(z)$  the nuclear stopping power in function of the depth (evaluated with SRIM software) and  $a = (1.19 \pm 0.11) \times 10^{15} \text{ cm}^{-2} \text{ keV nm}^{-1}$ . As explained in [34], the model from which Eq. 4 is derived leads to the estimation of the fraction of amorphized material at a given depth  $z$  in the sample, called “damage fraction”, i.e. the quantity which is integrated in Eq. 4. The total swelling at the surface of the sample can be considered as proportional to the integral of the damaged fraction over the full ion range.

The result of the comparison is reported in Figure 2c. Data for 8 MeV boron implantation are in good agreement with previous results.”

It is also worth focusing on the “edge swelling” height. Figure 2d shows the “edge swelling” height versus fluence from the regions irradiated at the same ion current of 500 pA (i.e. those labelled as A-I). The increase in the swelling height is less significant at higher fluences and it can be interpolated by eq. 5 (blue line).

$$height = \frac{a}{1 + e^{-k(fluence - x_c)}} \quad (5)$$

where the reported values are  $a = (192 \pm 15) \text{ nm}$ ,  $k = (27 \pm 7) \times 10^{-17} \text{ cm}^2$  and  $x_c = (85 \pm 9) \times 10^{14} \text{ ions cm}^{-2}$ . Figure 2e shows the dependence of the “edge swelling” height versus the current density while keeping a constant fluence value of  $10^{16} \text{ cm}^{-2}$  (i.e. regions labeled as J-L). In this case, for the explored parameter range, no significant dependence was observed.



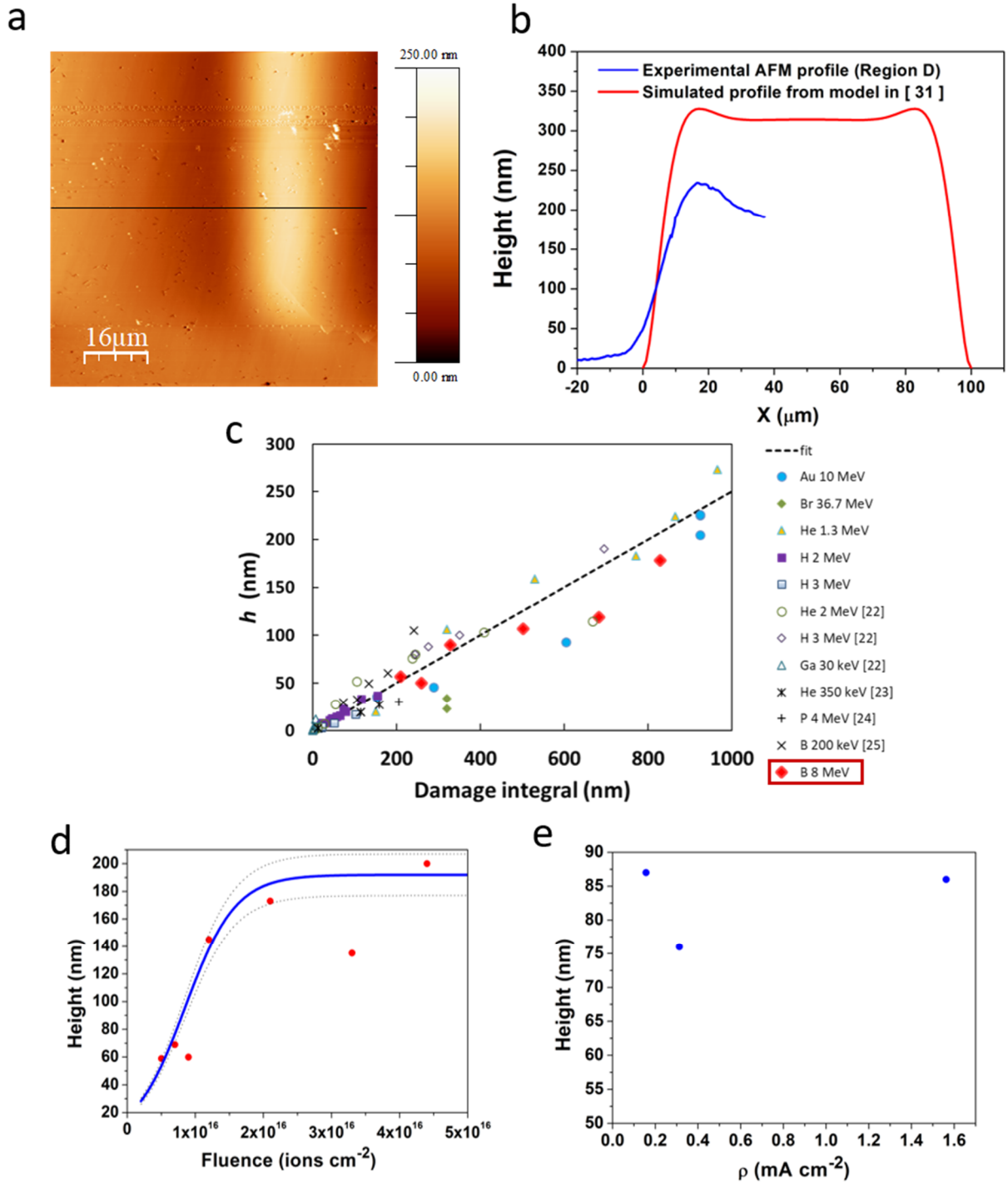


Figure 2: Swelling behaviour of the irradiated area with ion current 500 pA and fluence  $4.4 \times 10^{16} \text{ cm}^{-2}$ . a) AFM map of the edge of the irradiated square. b) comparison between the experimental cross-sectional AFM profile (blue line) extracted from the scan highlighted by a black line in the map (a) and the analytical profile developed in [31] (red line). c) "Plateau" swelling height versus the damage integral, compared with previous data. d) Edge swelling height versus fluence with constant ion current (500 pA). The blue line represents the interpolating function

(equation 5). e) Edge swelling height versus current density with constant fluence ( $10^{16} \text{ cm}^{-2}$ ); in this case, no significant dependence is observed.

### 3.2 Raman characterization

Raman spectroscopy was employed for a systematic structural characterization of the regions implanted at increasing fluences, both before and after the annealing process.

In order to assess both the spatial uniformity of the implanted regions and the use of single-spot spectra to perform the Raman characterization, we collected linear scans of the Raman spectra across the implanted areas, as shown in Figure 3a. Spectra for Raman profiles were collected with 1 s time acquisition (averaging 3 acquisitions). From each spectrum, the intensity of the first-order Raman diamond peak at  $1332 \text{ cm}^{-1}$  was estimated after proper background subtraction. A representative selection of results (for fluences of  $0.23 \times 10^{16} \text{ cm}^{-2}$ ,  $0.9 \times 10^{16} \text{ cm}^{-2}$  and  $3.3 \times 10^{16} \text{ cm}^{-2}$ ) are plotted in Figures 3b and 3c, which respectively correspond to the measurements performed before and after annealing. The peak intensity is constant across the same implanted region, showing the suitability of a study based on single-spot acquisitions. Before the thermal annealing, increasing fluence induces a decreasing intensity of the first-order Raman diamond peak. Following the high temperature thermal annealing, regions were irradiated at a fluence below the graphitization threshold are fully reconverted to diamond (as evident for region B, blue line in Figure 3c). Regions irradiated at fluences beyond the graphitization threshold show similar profiles of the Raman diamond peak intensity, since the diamond peak signal comes from the diamond “cap-layer” over the graphitized regions. As expected, the signal is less intense with respect to regions implanted below the graphitization threshold, because of the presence of the graphitized layer (where the laser is focused).

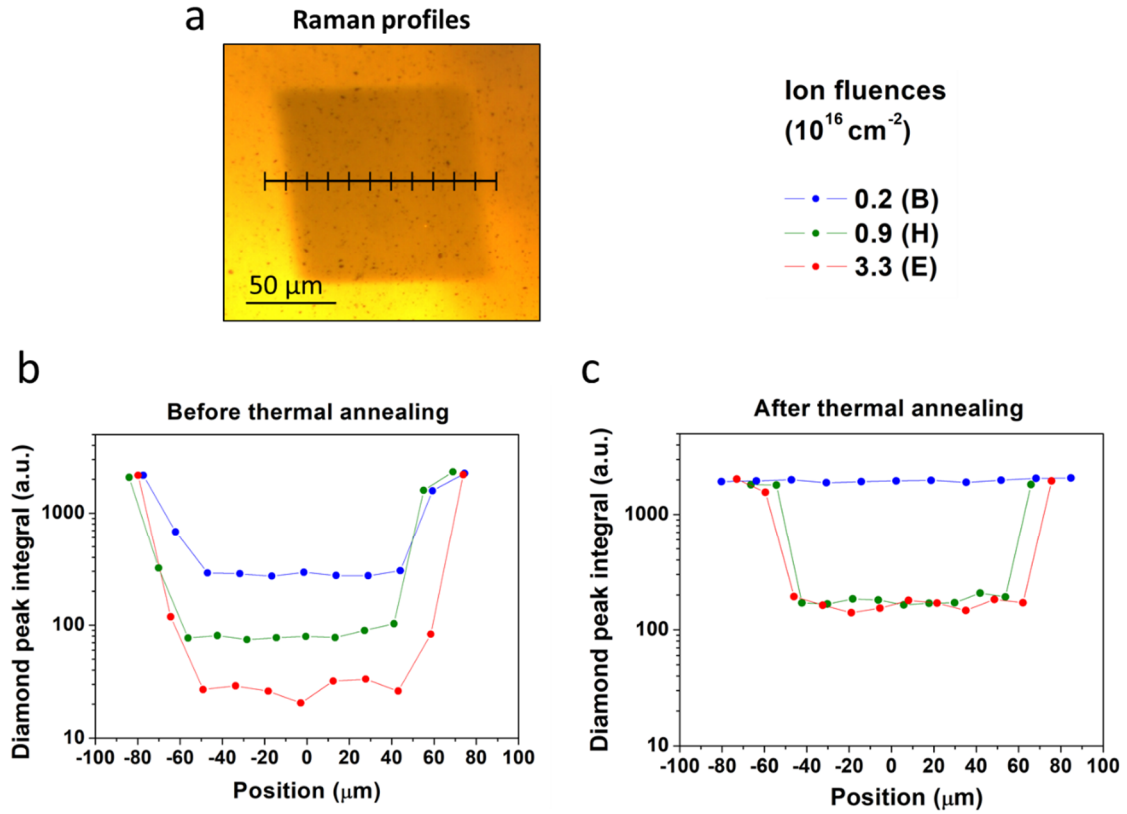


Figure 3: (a) Linear profile across the implanted region in the acquisition of the Raman spectra. Intensity of the first-order Raman diamond peak for a selection of representative regions (B, H and E), as acquired before (b) and after (c) thermal annealing.

The main observable feature in the Raman spectra collected from the different regions before thermal annealing is the first-order diamond peak at  $1332 \text{ cm}^{-1}$ . At the highest implantation fluences, low-intensity peaks appear at  $1500 \text{ cm}^{-1}$  and  $1635 \text{ cm}^{-1}$ , which are associated to general ion damaged diamond and  $\text{sp}^2$  and amorphous carbon phases (Figure 3a) [35].

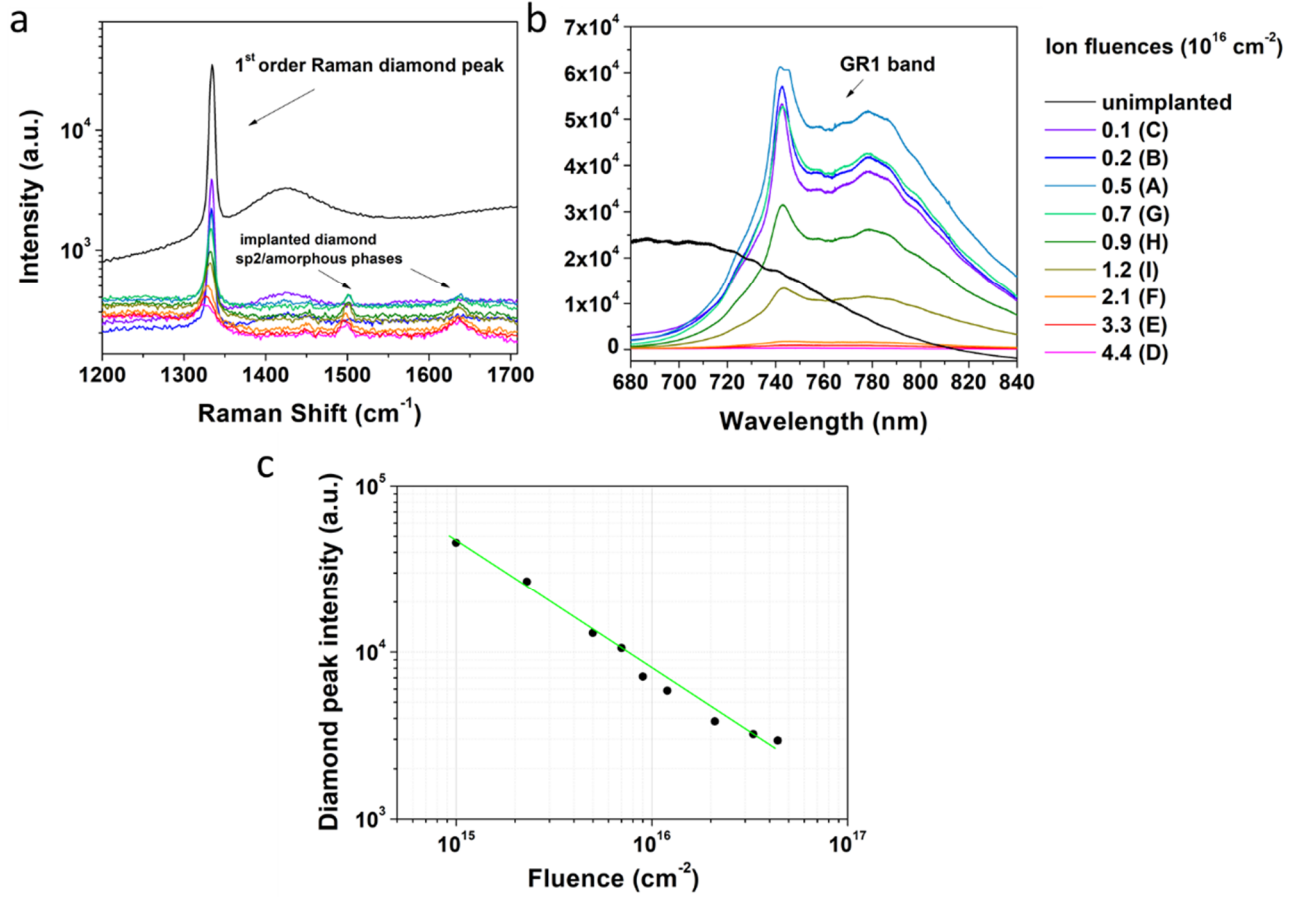


Figure 4 (a) Raman spectra collected from the irradiated areas before thermal annealing. The first-order diamond peak at  $1332 \text{ cm}^{-1}$  decreases in intensity as the fluence increases. (b) Photoluminescence spectra highlighting the GR1 emission feature associated with structural damage in diamond; while being absent in non-irradiated areas, the GR1 peak reaches its maximum intensity in the regions implanted at low fluences (C, B and A), then it decreases at higher fluences. (c) First-order diamond peak intensity in function of the implantation fluence; the uncertainty bar is included in the data point size.

It is also worth noting that a PL peak centered at  $1420 \text{ cm}^{-1}$  (corresponding to a 575 nm emission wavelength) associated to the  $\text{NV}^0$  centers is observable in the spectrum of the unimplanted crystal, while its intensity decreases until it disappears for higher implantation fluences, due to the introduction of PL quenching defects [36]. Photoluminescence bands appearing from 720 nm to 800 nm are ascribable to the GR1 center, which is a common PL spectral feature associated to individual vacancies in the diamond lattice [37]. The band is absent in the non-irradiated areas, while it is characterized by a high intensity in the regions implanted at the lowest fluences, with a maximum for a fluence value of  $5 \times 10^{15} \text{ cm}^{-2}$ . As observed in previous studies [35], the intensity of this PL feature progressively decreases at increasing boron concentrations, due to the compensation effect of the acceptors. Furthermore, the effect can also be attributed to the formation of vacancy complexes at higher damage densities [36]. Figure 4c shows the dependence of the intensity of the first-order Raman diamond peak from the irradiation fluence ( $F$ ). As the damage level increases, the peak intensity decreases with a  $\sim F^{-(0.77 \pm 0.04)}$  dependence. This result is qualitatively consistent with what was obtained in previous studies [38] for 60 keV  $\text{B}_2$  implantation, for which a  $\sim F^{-1}$  dependence was observed in the same damage range, although

with a more pronounced data scattering. The discrepancy between the power-law trends could be attributed to the significantly different boron implantation energies (i.e. 30 keV and 8 MeV, respectively), which determine different damage profiles.

The Raman spectra collected from the annealed sample (Figure 5a) are characterized by several features, which can be summarized as follows:

- First-order Raman diamond peak at  $1332\text{ cm}^{-1}$ . As showed in Figure 4b, the intensity of this feature (after proper subtraction of the G-band background) decreases as the fluence increases, with a clearly defined collapse in correspondence of a fluence of  $5 \times 10^{15}\text{ cm}^{-2}$ , at which the graphitization threshold is reached. The feature is still visible in the spectra acquired from the graphitized regions, since it arises from the diamond “cap layer” comprised between the graphitized layer and the sample surface (it is worth remarking that the focal resolution in depth is  $\sim 3\text{ }\mu\text{m}$ ).
- The Raman “G band” centered at  $1550\text{ cm}^{-1}$ , which is indicative of disordered and graphite-like  $\text{sp}^2$  phases. Complementarily with what is observed for the first-order diamond line, this feature is absent in the unimplanted regions as well as from the areas implanted at low (i.e.  $< 5 \times 10^{15}\text{ cm}^{-2}$ ) fluences, while its intensity progressively increases at larger fluences. More in detail, the G band intensity has a linear dependence from the values of the graphitic layer thickness that were estimated as described in the “Materials and Methods” Section. This is confirming that i) the stronger Raman signal can be suitably attributed to an increase of the graphitized volume, and ii) the procedure that was adopted to estimate the thickness of the graphitic layers on the basis of the graphitization threshold value is reliable, at least in first approximation.
- $\text{NV}^0$  and  $\text{NV}^-$  ZPL peaks at 575 nm and 638 nm, respectively, followed at larger wavelengths by the respective phonon sidebands. These features are observed only from the unimplanted regions as well as from the areas implanted at low fluences (i.e.  $< 7 \times 10^{15}\text{ cm}^{-2}$ ). At higher fluences, a significant reduction of the NV PL emission is accompanied by a strong modulation of the spectral emission with periodic interference peaks which are attributed to multiple internal reflections of the emitted radiation across cap layer, as already observed in previous works [37].

With regards to the latest spectral feature, it is possible to estimate the thickness of the cap layer from the period of the interference pattern at normal incidence, using the formula [39]:

$$d = \frac{1}{2 \cdot n \cdot \left[ \left( \frac{1}{\lambda_1} \right) - \left( \frac{1}{\lambda_2} \right) \right]} \quad (6)$$

where  $d$  is the layer thickness,  $n(\lambda)$  is the refractive index of diamond, and  $\lambda_{1,2}$  are the wavelengths corresponding to two consecutive maxima (or minima) in the interference pattern. The resulting thickness is  $d = (4.6 \pm 0.3)\text{ }\mu\text{m}$ , assuming a refractive index of 2.42 [40].

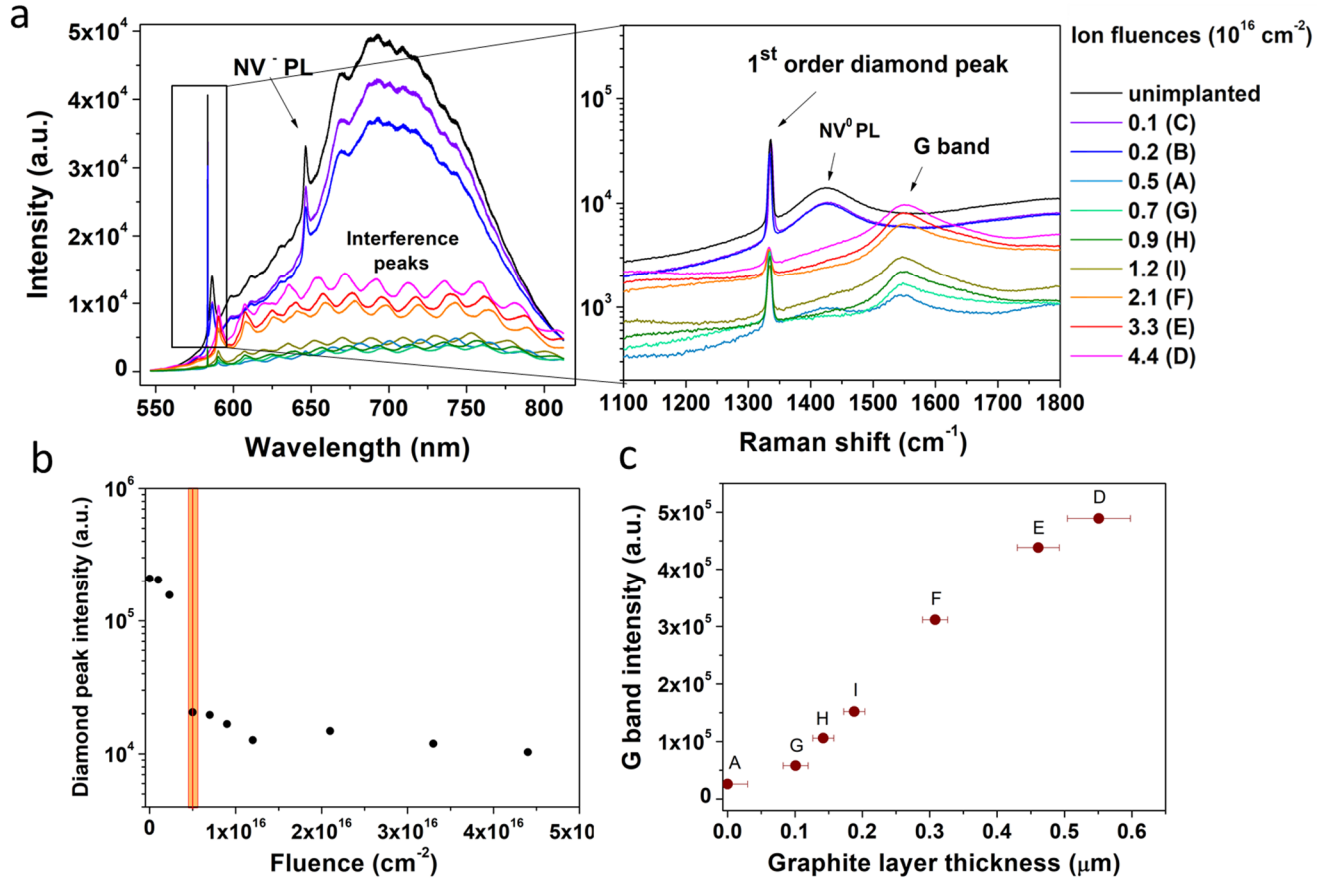


Figure 5: Raman/PL characterization of the sample after thermal annealing. (a) PL spectra collected from the irradiated areas and zoom-in of the spectral range over which the Raman features are observed. (b) First-order Raman diamond peak intensity in function of the implantation fluence: a sharp decrease is evident in correspondence of the region implanted at the fluence for which the graphitization threshold is overcome (red line); error bar included in the datapoint size. (c) Raman G band intensity in function of the graphitic layer thickness evaluated as described in the “Materials and Methods” Section.

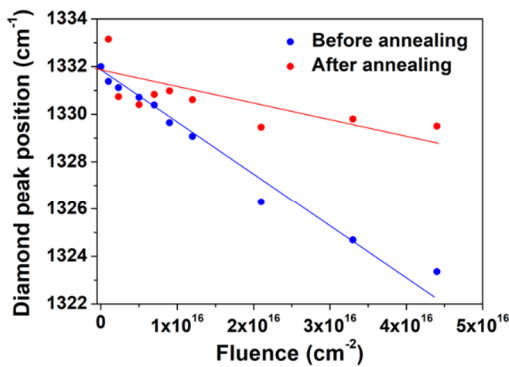
Figure 6a reports the position of the first-order Raman diamond peak in function of the fluence, as measured both before and after the thermal annealing. The linear variation of the peak position to lower Raman shift values at increasing damage densities is less pronounced after annealing. This is interpreted as due to the fact that the thermal processing allows a substantial recovery of the pristine crystal structure (thus strongly reducing the shift effect on the Raman spectra) while at the same time a finite amount of residual damage does not allow a complete recovery of the first-order Raman peak position to its initial value. Analogously, the width of the first-order diamond Raman peak (which was estimated as a FWHM (Full Width at Half Maximum) value) exhibits a progressive increase with the fluence (Figure 5b), and also in this case the variation is less pronounced for the sample after thermal annealing, thus corroborating our interpretation based on a substantial (but nonetheless incomplete) recovery of the crystal structure upon thermal processing. Following the interpretation formulated in [20], the progressive increase in the width of the first-order diamond Raman peak associated to the increasing structural damage can be attributed to the decrease in phonon lifetime as a result of the scattering from the ion-induced defects. In correspondence of the probed  $1332\text{ cm}^{-1}$  Raman transition, the zone center unperturbed phonon frequency acquires a complex shift: while the imaginary part (i.e. the linewidth which is inversely proportional to the phonon lifetime) increases, the real part is

subjected to a redshift, as described by the Kramers-Kronig relationships that correlate these quantities in the anharmonic approximation that is applicable to diamond [41]. Hence, this interpretation can explain the redshift in the peak position as well as the concurrent increase of the peak width. Remarkably, in both of the above-mentioned linear variations, a change in the slope is observable in correspondence of a fluence value comprised within the  $1\text{-}2 \times 10^{16} \text{ cm}^{-2}$  range, which roughly corresponds to the graphitization threshold [20].

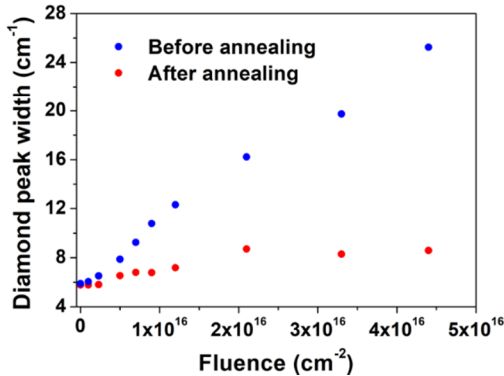
In Figure 6c the width of the first-order Raman line was plotted in function of its centroid. The linear correlation between these parameters is consistent with the one obtained for diamond samples implanted with 3 MeV alpha particles [20], with a remarkable data overlap in our investigated range (identifying the same angular coefficient, being approximately  $\sim 2$ ). This is indicative of a general Kramers-Kronig trend, which is independent from the type and energy of damaging radiation.

As shown in Figure 6c, even after the thermal process, the width/centroid relationship after appears compatible with the previous data; however the narrow range of data due to the reduction of structural effects within the cap layer induced by thermal annealing, prevents any further data interpretation.

a



b



c

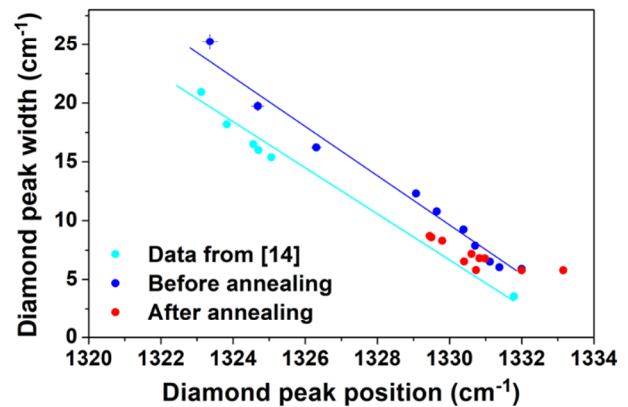


Figure 6: (a) First-order diamond Raman peak position in function of the fluence; the blue and red lines represent the linear fits of the respective data before and after annealing. (b) First-order diamond Raman peak width in function of the fluence before (blue) and after (red) annealing. (c) Relationship between the width and position of the first-order Raman diamond peak; data from [20] are reported in cyan.

In Figure 7 we report Raman spectra acquired from regions implanted at a fixed fluence of  $1 \times 10^{16} \text{ cm}^{-2}$  (i.e. beyond the graphitization threshold), while varying the ion beam current (50 pA, 100 pA and 500 pA). The study of different dose rate is conducted in order to investigate possible self-annealing effects occurring during the irradiation. In the spectra that were acquired before thermal annealing, both the first order Raman diamond peak at  $1332 \text{ cm}^{-1}$  (Figure 6a) and GR1 photoluminescence band (Figure 6b) appear slightly more intense at 100 pA and 500 pA with respect to the spectrum at 50 pA. A possible interpretation for this experimental evidence could be based on the fact that at higher ion beam currents (100 pA and 500 pA), self-thermal heating occurring during the ion irradiation promotes the migration of the vacancies and consequently it reduces the formation of vacancy complexes, determining a more pronounced GR1 emission for high implantation currents. Thus, we can conclude that adopting higher currents can be effective in slightly reducing the detrimental damage effect occurring during the ion implantation-based doping.

Similarly, to the results presented for the other implanted regions, upon high-temperature thermal annealing the GR1 feature disappears. Periodic interference peaks appear, due to the multiple reflections of the outgoing radiation in the diamond “cap-layer” located above the graphitized regions (Figure 6c).

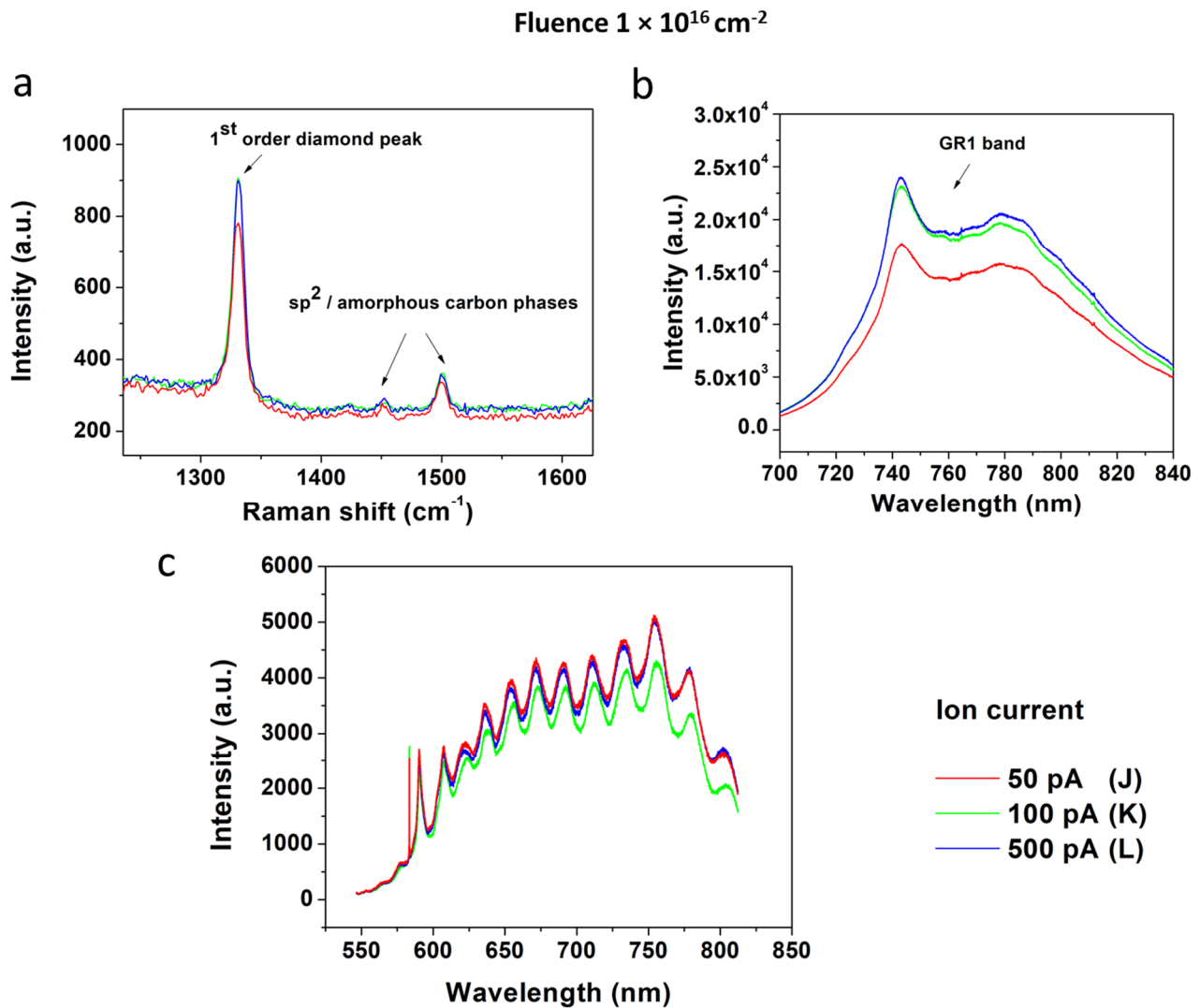




Figure 7: (a) Raman spectra of regions J, K and L before thermal annealing. (b) PL spectra of GR1 band of regions J, K and L before thermal annealing. (c) PL spectra collected from regions J, K and L after thermal annealing.

## Conclusions

An optical-grade type IIa monocrystalline diamond sample was implanted with a focused 8 MeV  $^{11}\text{B}$  ion beam. Different square-shaped areas were exposed to increasing fluences (from  $1 \times 10^{15} \text{ cm}^{-2}$  to  $4.4 \times 10^{16} \text{ cm}^{-2}$ ).

A morphological characterization by means of Atomic Force Microscopy of a not-annealed sample allowed the measurement of the well-known swelling effect, while highlighting edge effects occurring at the borders of the implanted areas, which are still poorly understood despite several reports appeared in a limited series of previous works [29–32]. AFM results were compared with previous theoretical prediction developed with analytical methods [31]. The extension of the “lip” on both Z and X-axis appears comparable with the expectations. However, the overall AFM profile is not fully in line with the theoretical prediction, probably because of the theoretical model is based on an annealed sample incorporating a sharply defined region embedded in a pristine diamond matrix.

A systematic Raman characterization of the implanted areas was performed, in particular focusing on the first order Raman diamond peak, evaluating its intensity, width and position at different implantation conditions. Our data are consistent with what obtained in previous studies for different implanted species and different energies, confirming the same connection between this Raman feature and the damage level in the diamond lattice, in qualitative agreement with the formalism of the Kramers-Kronig relationships. A further characterization following a high thermal annealing, allowed to study the residual damage and to define the graphitization threshold at a fluence of  $5 \times 10^{15} \text{ cm}^{-2}$ , corresponding to a vacancy density of  $\sim 4.4 \times 10^{22} \text{ vacancies cm}^{-3}$  as obtained in a simple linear approximation. This value is well in line with previous results, and allowed an estimation of the thickness of the formed graphitic layers. Such estimation appeared consistent with the measured evolution of the intensity of the Raman G band. The Raman characterization of the regions implanted at a fixed fluence and variable ion beam current showed the potential advantage of using higher currents to slightly limit the sample damage due to this doping method.

## Acknowledgement

The present work was supported by the Grant "Departments of Excellence" (L. 232/2016), funded by the Italian Ministry of Education, University and Research (MIUR), by the Italian Institute for Nuclear Physics (INFN) within the experiments "ASIDI" and "DIACELL" and by CRT foundation within the MiRaDS project. The authors wish to thank the technical staff of CMAM for operating the tandem.

## Bibliography

- [1] J.E. Moussa, M.L. Cohen, Constraints on  $T_c$  for superconductivity in heavily boron-doped diamond, *Phys. Rev. B - Condens. Matter Mater. Phys.* 77 (2008) 1–8. doi:10.1103/PhysRevB.77.064518.
- [2] F. Fontaine, E. Gheeraert, a. Deneuve, Conduction mechanisms in boron implanted diamond films, *Diam. Relat. Mater.* 5 (1996) 752–756. doi:10.1016/0925-9635(95)00383-5.
- [3] T. Vogel, J. Meijer, A. Zaitsev, Highly effective p-type doping of diamond by MeV-ion implantation of boron, *Diam. Relat. Mater.* 13 (2004) 1822–1825. doi:10.1016/j.diamond.2004.04.005.
- [4] L.H. Willems Van Beveren, R. Liu, H. Bowers, K. Ganesan, B.C. Johnson, J.C. McCallum, S. Prawer, Optical and electronic properties of sub-surface conducting layers in diamond created by MeV B-implantation at elevated temperatures, *J. Appl. Phys.* 119 (2016) 1–7. doi:10.1063/1.4953583.
- [5] D.L. Creedon, Y. Jiang, K. Ganesan, A. Stacey, T. Kageura, H. Kawarada, J.C. McCallum, B.C. Johnson, S. Prawer, D.N. Jamieson, Irradiation-Induced Modification of the Superconducting Properties of Heavily-Boron-Doped Diamond, *Phys. Rev. Appl.* 10 (2018) 1. doi:10.1103/PhysRevApplied.10.044016.
- [6] C. Uzansaguy, C. Cytermann, R. Brener, V. Richter, M. Shaanan, R. Kalish, Damage Threshold for Ion-Beam-Induced Graphitization of Diamond, *Appl. Phys. Lett.* 67 (1995) 1194–1196. doi:10.1063/1.115004.
- [7] A. Battiato, M. Lorusso, E. Bernardi, F. Picollo, F. Bosia, D. Ugues, A. Zelferino, A. Damin, J. Baima, N.M. Pugno, E.P. Ambrosio, P. Olivero, Softening the ultra-stiff: Controlled variation of Young's modulus in single-crystal diamond by ion implantation, *Acta Mater.* 116 (2016) 95–103. doi:10.1016/j.actamat.2016.06.019.
- [8] D.P. Hickey, K.S. Jones, R.G. Elliman, Amorphization and graphitization of single-crystal diamond - A transmission electron microscopy study, *Diam. Relat. Mater.* 18 (2009) 1353–1359. doi:10.1016/j.diamond.2009.08.012.
- [9] A. Gippius, R.A.R. Khmel'nitskiy, V.A. Dravin, S.D. Tkachenko, Formation and characterization of graphitized layers in ion-implanted diamond, *Diam. Relat. Mater.* 8 (1999) 1631–1634. doi:10.1016/S0925-9635(99)00047-3.
- [10] J.F. Prins, Onset of hopping conduction in carbon ion-implanted diamond, *Phys. Rev. B.* 31 (1985) 2472–2478.
- [11] J.F. Prins, Fermi-Dirac statistics and the nature of the compensating donors in boron-doped diamond layers, *Phys. Rev. B.* 39 (1989) 3764–3770. doi:10.1103/PhysRevB.39.3764.
- [12] R. Kalish, C. Uzan-Saguy, A. Samoiloff, R. Locher, P. Koidl, Doping of polycrystalline diamond by boron ion implantation, *Appl. Phys. Lett.* 64 (1994) 2532–2534. doi:10.1063/1.111564.
- [13] S. Mandal, T. Bautze, O.A. Williams, C. Naud, É. Bustarret, F. Omnès, P. Rodière, T. Meunier, C. Bäuerle, L. Saminadayar, The Diamond Superconducting Quantum Interference Device, *ACS Nano.* 5 (2011) 7144–7148. doi:10.1021/nn2018396.
- [14] J.F. Prins, Activation of boron-dopant atoms in ion-implanted diamonds, *Phys. Rev. B.* 38 (1988) 5576–5584. doi:10.1103/PhysRevB.38.5576.
- [15] S. Prawer, R. Kalish, Ion-beam-induced transformation of diamond, *Phys. Rev. B.* 51 (1995) 15711–15722. doi:10.1103/PhysRevB.51.15711.
- [16] R. Kalish, a. Reznik, S. Prawer, D. Saada, J. Adler, Ion-Implantation-Induced Defects in Diamond and Their Annealing: Experiment and Simulation, *Phys. Status Solidi.* 174 (1999) 83–99. doi:10.1002/(SICI)1521-396X(199907)174:1<83::AID-PSSA83>3.0.CO;2-3.

- [17] J.D. Hunn, S.P. Withrow, C.W. White, D.M. Hembree, Raman scattering from MeV-ion implanted diamond, *Phys. Rev. B.* 52 (1995) 8106–8111. doi:10.1103/PhysRevB.52.8106.
- [18] D.N.N. Jamieson, S. Prawer, K.W.W. Nugent, S.P.P. Dooley, Cross-sectional Raman microscopy of MeV implanted diamond, *Nucl. Inst. Methods Phys. Res. B.* 106 (1995) 641–645. doi:10.1016/0168-583X(96)80036-X.
- [19] a. a. Bergman, a. M. Zaitsev, M. Huang, a. a. Gorokhovskiy, Photoluminescence and Raman studies of Xe ion-implanted diamonds: Dependence on implantation dose, *J. Lumin.* 129 (2009) 1524–1526. doi:10.1016/j.jlumin.2008.11.028.
- [20] J.O. Orwa, K.W. Nugent, D.N. Jamieson, S. Prawer, Raman investigation of damage caused by deep ion implantation in diamond, *Phys. Rev. B - Condens. Matter Mater. Phys.* 62 (2000) 5461–5472. doi:10.1103/PhysRevB.62.5461.
- [21] F. Agulló-Rueda, M.D. Ynsa, N. Gordillo, A. Maira, D. Moreno-Cerrada, M.A. Ramos, Micro-Raman spectroscopy of near-surface damage in diamond irradiated with 9-MeV boron ions, *Diam. Relat. Mater.* 72 (2017) 94–98. doi:10.1016/j.diamond.2017.01.010.
- [22] M.D. Ynsa, M.A. Ramos, N. Skukan, V. Torres-Costa, M. Jakšić, Highly-focused boron implantation in diamond and imaging using the nuclear reaction  $^{11}\text{B}(p, \alpha)^8\text{Be}$ , *Nucl. Instruments Methods Phys. Res. Sect. B Beam Interact. with Mater. Atoms.* 348 (2015) 174–177. doi:10.1016/j.nimb.2014.11.036.
- [23] J.F. Ziegler, M.D. Ziegler, J.P. Biersack, SRIM - The stopping and range of ions in matter (2010), *Nucl. Instruments Methods Phys. Res. Sect. B Beam Interact. with Mater. Atoms.* 268 (2010) 1818–1823. doi:10.1016/j.nimb.2010.02.091.
- [24] W. Wu, S. Fahy, Molecular-dynamics study of single-atom radiation damage in diamond, *Phys. Rev. B.* 49 (1994) 3030–3035. doi:10.1103/PhysRevB.49.3030.
- [25] F. Bosia, N. Argiolas, M. Bazzan, B. a Fairchild, a D. Greentree, D.W.M. Lau, P. Olivero, F. Picollo, S. Rubanov, S. Prawer, Direct measurement and modelling of internal strains in ion-implanted diamond., *J. Phys. Condens. Matter.* 25 (2013) 385403. doi:10.1088/0953-8984/25/38/385403.
- [26] E.K.K. Nshingabigwi, T.E.E. Derry, S.R.R. Naidoo, J.H.H. Neethling, E.J.J. Olivier, J.H.H. O’Connell, C.M.M. Levitt, Electron microscopy profiling of ion implantation damage in diamond: Dependence on fluence and annealing, *Diam. Relat. Mater.* 49 (2014) 1–8. doi:10.1016/j.diamond.2014.07.010.
- [27] I. Horcas, R. Fernández, J.M. Gómez-Rodríguez, J. Colchero, J. Gómez-Herrero, A.M. Baro, <sc>WSXM</sc> : A software for scanning probe microscopy and a tool for nanotechnology, *Rev. Sci. Instrum.* 78 (2007) 013705. doi:10.1063/1.2432410.
- [28] J.F. Prins, T.E. Derry, J.P.F. Sellschop, Volume expansion of diamond during ion implantation, *Phys. Rev. B.* 34 (1986) 8870–8874. doi:10.1103/PhysRevB.34.8870.
- [29] F. Bosia, S. Calusi, L. Giuntini, S. Lagomarsino, A. Lo Giudice, M. Massi, P. Olivero, F. Picollo, S. Sciortino, A. Sordini, M. Vannoni, E. Vittone, Finite element analysis of ion-implanted diamond surface swelling, *Nucl. Instruments Methods Phys. Res. Sect. B Beam Interact. with Mater. Atoms.* 268 (2010) 2991–2995. doi:10.1016/j.nimb.2010.05.025.
- [30] F. Bosia, N. Argiolas, M. Bazzan, P. Olivero, F. Picollo, a. Sordini, M. Vannoni, E. Vittone, Modification of the structure of diamond with MeV ion implantation, *Diam. Relat. Mater.* 20 (2011) 774–778. doi:10.1016/j.diamond.2011.03.025.
- [31] M. Piccardo, F. Bosia, P. Olivero, N. Pugno, An analytical model for the mechanical deformation of locally graphitized diamond, *Diam. Relat. Mater.* 48 (2014) 73–81. doi:10.1016/j.diamond.2014.07.006.
- [32] G. García, I. Preda, M. Díaz-Híjar, V. Tormo-Márquez, O. Peña-Rodríguez, J. Olivares, F. Bosia, N.M. Pugno, F. Picollo, L. Giuntini, A. Sordini, P. Olivero, L. López-Mir, C. Ocal, Micro

and nano-patterning of single-crystal diamond by swift heavy ion irradiation, *Diam. Relat. Mater.* 69 (2016) 1–7. doi:10.1016/j.diamond.2016.06.015.

- [33] a. V. Khomich, R.A. Khmel'nitskiy, V.A. Dravin, a. a. Gippius, E. V. Zavedeev, I.I. Vlasov, Radiation damage in diamonds subjected to helium implantation, *Phys. Solid State.* 49 (2007) 1661–1665. doi:10.1134/S1063783407090107.
- [34] G. García, M. Díaz-Híjarb, V. Tormo-Márquez, I. Preda, O. Peña-Rodríguez, J. Olivares, Erratum: Structural damage on single-crystal diamond by swift heavy ion irradiation, *Diam. Relat. Mater.* 59 (2015) 122. doi:10.1016/j.diamond.2015.10.012.
- [35] A.M. Zaitsev, *Optical properties of diamond: a data handbook*, 2001. doi:10.1007/978-3-662-04548-0.
- [36] F.C. Waldermann, P. Olivero, J. Nunn, K. Surmacz, Z.Y. Wang, D. Jaksch, R.A. Taylor, I.A. Walmsley, M. Draganski, P. Reichart, A.D. Greentree, D.N. Jamieson, S. Prawer, Creating diamond color centers for quantum optical applications, *Diam. Relat. Mater.* 16 (2007) 1887–1895. doi:10.1016/j.diamond.2007.09.009.
- [37] P. Olivero, S. Rubanov, P. Reichart, B.C. Gibson, S.T. Huntington, J.R. Rabeau, A.D. Greentree, J. Salzman, D. Moore, D.N. Jamieson, S. Prawer, Characterization of three-dimensional microstructures in single-crystal diamond, *Diam. Relat. Mater.* 15 (2006) 1614–1621. doi:10.1016/j.diamond.2006.01.018.
- [38] H. Amekura, N. Kishimoto, Effects of high-fluence ion implantation on colorless diamond self-standing films, *J. Appl. Phys.* 104 (2008). doi:10.1063/1.2978215.
- [39] M. Born, E. Wolf, *Principles of Optics*, 6th ed., 1980.
- [40] A. Battiato, F. Bosia, S. Ferrari, P. Olivero, A. Sytchkova, E. Vittone, Spectroscopic measurement of the refractive index of ion-implanted diamond, *Opt. Lett.* 37 (2012) 671–673. doi:10.1364/OL.37.000671.
- [41] M. Liu, L. Bursill, S. Prawer, R. Beserman, Temperature dependence of the first-order Raman phonon line of diamond, *Phys. Rev. B.* 61 (2000) 3391–3395. doi:10.1103/PhysRevB.61.3391.